

## SUPPLEMENTARY METHODS 1: IRSL MEASUREMENTS

---

### Sample cutting

Rock samples were sawed under dim, indirect amber lighting conditions using a water-cooled, low-speed lapidary saw. All three bedrock samples were sliced perpendicular to the ground surface. During initial sample collection, the drill intersected the bedrock at acute angles, so the maximum recoverable depth of these samples with a known distance-to-surface was limited to 42 and 47 mm for cores H1 and H4, respectively (Table S2). Sample KAY-110 was taken from a bedrock surface 21 m above the ice margin on Kay Peak Ridge that had previously been sampled for exposure-dating purposes (Figure 1). In 2016, a rock saw was used to remove several blocks from the rock surface, thereby exposing previously unbleached rock to sunlight. Sample KAY-110 projected above the surrounding rock (Figure 1a) during its exposure to sunlight for 4 years and was detached from the boulder during the 2020 field season. For this sample, the peripheral 2 cm of rock was sawn off prior to slicing the interior rock fragment, to remove any sunlight bleaching influence from the side of the depth profile (Figure 1b).

We were also limited by the minimum rock size that could be secured for cutting. As a result, the bottom-most piece of H1 is 5 mm thick. For core H4, during an initial cut, the deeper portion broke away from the shallower portion at a depth of about 27 mm. We therefore sliced the shallow piece into ~1.5-mm-thick segments to a depth of 18.7 mm, then used the piece from 19.1 to 26.9 mm and the piece from 26.9 to 46.6 mm.

We performed cuts at 1.5-mm increments by advancing a set screw within a jig clamped to the cross-feed of the saw. The blade thickness is 0.38 mm. The top and bottom depths of each slice are listed in Table S2, as determined by repeat digital caliper measurements of both the individual slices and the remaining core segment.

### Luminescence measurements

Each rock slice was broken approximately into quarters. Three of four quarter fragments at each depth were gently and separately crushed by pestle and mortar to disaggregate the grains which were mounted onto aluminum aliquots with a ~2 mm monolayer spot size. Each measured aliquot therefore represents one quadrant of a given depth slice. The purpose of measuring the luminescence response of quadrants separately rather than amalgamating all material within a given slice is to better capture the natural variability in latent luminescence at each depth (Sellwood et al., 2019).

Luminescence measurements were performed on a TL-DA-20 Risø automated luminescence reader equipped with a  $^{90}\text{Sr}/^{90}\text{Y}$  beta source that delivers 0.1 Gy/s at the sample location (Bøtter-Jensen et al., 2003). Emissions were detected through a Schott BG3-BG39 filter combination. We used a post-infrared infrared-stimulated luminescence (pIRIR) protocol (Buylaert et al., 2009) to determine the sensitivity-corrected natural luminescence intensities ( $L_N/T_N$ ) as well as the dose response and fading characteristics of samples (Table S2). With this pIRIR protocol we measure two luminescence: the more bleachable  $\text{IR}_{50}$  signal, which has higher signal fading rates, and the less bleachable pIRIR<sub>225</sub> signal, which fades less. We assume that the  $\text{IR}_{50}$  emissions originate from both Na- and K-rich feldspars and that the pIRIR<sub>225</sub> signal is mostly from K-rich feldspars (Thomsen et al., 2018).

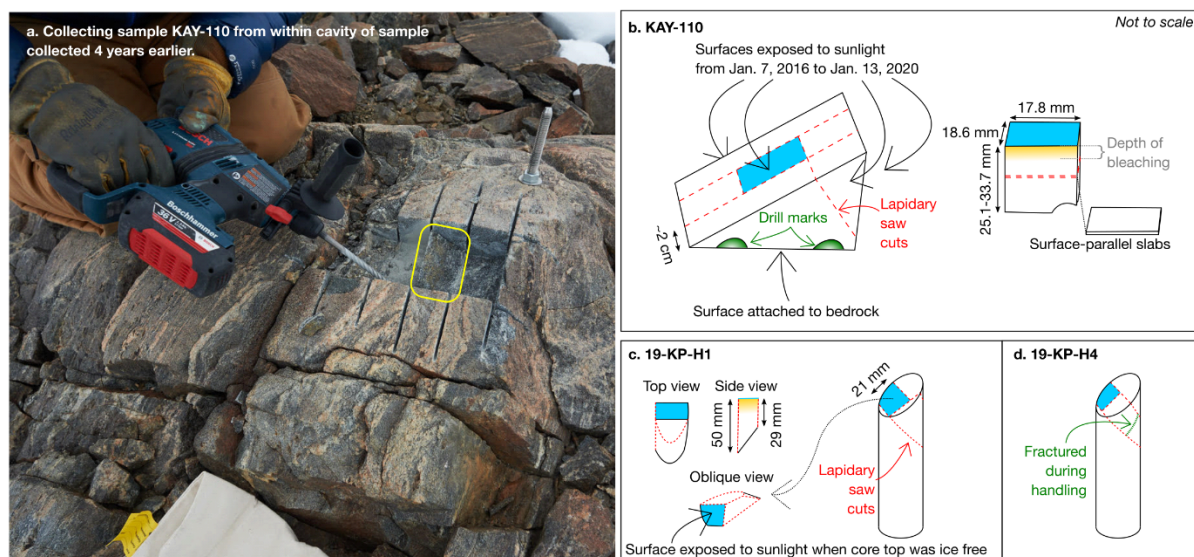


**Figure 1:** (a) Photo of sample KAY-110 being collected from within a hole created in 2016. The rock fragment analyzed here is outlined in yellow. (b) The sunlight-exposed perimeter of the KAY-110 rock fragment was removed and the remaining interior piece was slabbed parallel to the surface. The 19-KP-H1 (c) and 19-KP-H4 (b) core tops were also slabbed parallel to the surface. Because the coring drill entered the bedrock at an acute angle, slabs were collected to surface-perpendicular depths of 36.6 and 26.9 mm for H1 and H4, respectively.

## Geologic dose rate

The geologic dose rates for core top samples and 19-KP-H4 were estimated from the whole rock elemental composition of the depth interval directly beneath the luminescence depth profile: 6.0-7.0 cm for 19-KP-H1 and 5.7-7.5 cm for 19-KP-H4. The Washington State University GeoAnalytical Lab performed X-ray fluorescence (XRF) and inductively coupled plasma mass spectrometry (ICP-MS) measurements which agree within uncertainties, though ICP-MS values are used for dose rate calculations (Table S2).

The infinite matrix dose rate was calculated with the DRAC online calculator (v1.2) (Durcan et al., 2015). We assumed: an internal K content of  $12.5 \pm 0.5$  wt. % (Huntley and Baril, 1997); a grain size of  $750 \pm 250$   $\mu\text{m}$ , based on thin section analysis;  $35 \pm 5$  m of overburden with density  $0.917 \pm 0.1$   $\text{g/cm}^3$ ; rock water content of  $0 \pm 1$  %; and an alpha efficiency factor of  $0.15 \pm 0.05$  (Balescu and Lamothe, 1994). We used the radionuclide conversion factors of Liritzis et al. (2013) and alpha and beta grain attenuation factors of Brennan et al. (1991) and Guérin et al. (2012), respectively. The depth dependent dose rate was calculated using gamma and beta attenuation factors of 0.02 and 1.9  $\text{mm}^{-1}$  (Sohbati et al., 2015). Results are shown in **Figure 2**.

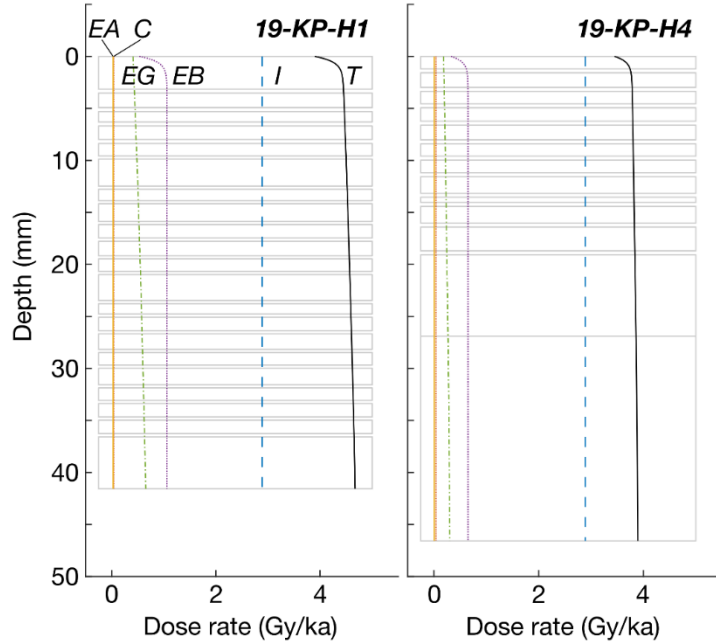


**Figure 2:** The total geologic dose rate ( $T$ ) for both core top samples, comprised of the external alpha ( $EA$ ), external beta ( $EB$ ), external gamma ( $EG$ ), cosmic ( $C$ ), and internal ( $I$ ) dose rate components, where external and internal refer to radiation originating outside of or within the grain.

### Bedrock bleaching characteristics

With luminescence measurements on the 19-KP-H1 and 19-KP-H4 core top samples, we determine whether either of these bedrock surfaces was exposed to sunlight on timescales less than field saturation, which for these samples we estimate at 196 to 276 ka (see following section for details). If either core were exposed to sunlight, the natural luminescence intensity would be reduced to zero at the rock surface and then to greater depths with time. The depth of bleaching would increase in proportion to the logarithm of sunlight exposure time until eventually the charge detrapping rate by bedrock-attenuated sunlight equaled the charge trapping rate by environmental radiation (Sohbati et al., 2012; Sohbati et al., 2018). The bleaching rate with depth relationship is sample dependent (Meyer et al., 2018; Ou et al., 2018), and should be calibrated against a known-age surface. For the present study, we use sample KAY-110 (**Figure 1a**), which was exposed to sunlight for 4 years prior to collection.

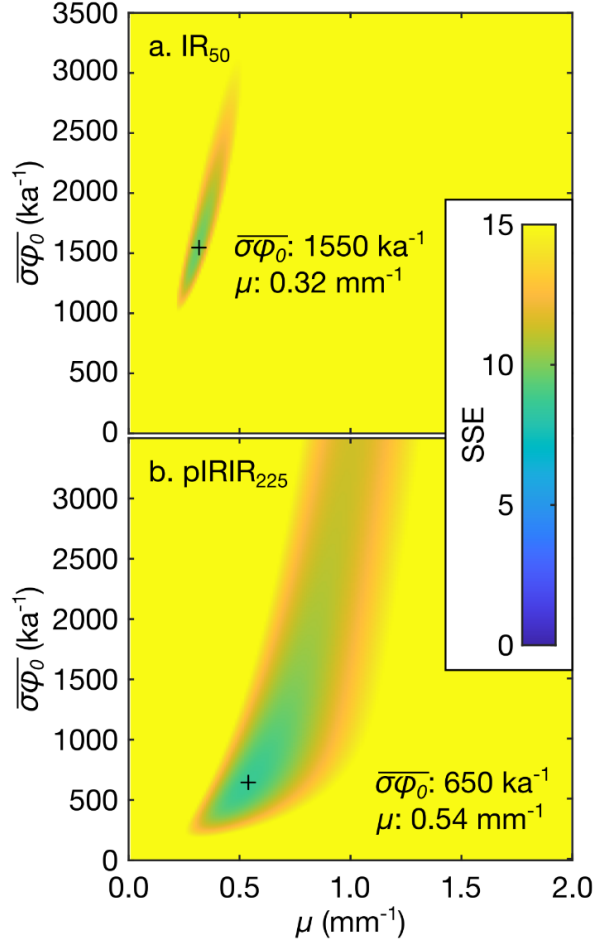


**Figure 3:** Weighted sum of squares misfit (SSE) between observed  $L_N/T_N$  values for sample KAY-110 after 4 years of sunlight exposure (Fig. 2 of main text) and values of  $L_N/T_N$  simulated with Eq. 1. The best-fit kinetic parameters are located with '+' symbols next to the corresponding values.

The IR<sub>50</sub> and pIRIR<sub>225</sub> depth profiles for KAY-110 (Fig. 6 of main text) show reduced  $L_N/T_N$  ratios near the sunlight exposed surface, consistent with known sunlight exposure. These profiles were fitted to the expression of Sohbaty et al. (2012):

$$\frac{n(x,t)}{N} = \frac{E(x)e^{-t[E(x)+F]} + F}{E(x) + F} \quad \text{Eq. 1}$$

where  $n/N$  is fractional saturation;  $F$  is the trapping rate constant ( $\text{ka}^{-1}$ ), dependent on the environmental dose rate,  $\dot{D}$  (Gy/ka), and the characteristic dose  $D_0$  (Gy):

$$F = \dot{D}/D_0 \quad \text{Eq. 2}$$

and  $E(x)$  is the detrapping rate constant ( $\text{ka}^{-1}$ ) at depth  $x$  (mm):

$$E(x) = \overline{\sigma\varphi_0} e^{-\mu x} \quad \text{Eq. 3}$$

where  $\overline{\sigma\varphi_0}$  is the mean detrapping rate constant at the rock surface ( $\text{ka}^{-1}$ ) and  $\mu$  is the sunlight attenuation coefficient ( $\text{mm}^{-1}$ ). In the context of  $L_N/T_N$  bleaching profiles of known age surfaces,  $N$  (for geologic dose rates) is proportional to the mean  $L_N/T_N$  ratio at unbleached depths and  $t$  is the known sunlight exposure duration. A series of  $\text{IR}_{50}$  and  $\text{pIRIR}_{225}$   $L_N/T_N$  profiles were generated for all values  $\overline{\sigma\varphi_0}$  from 10 to 3500  $\text{ka}^{-1}$  incremented by 5  $\text{ka}^{-1}$  and values of  $\mu$  from 0.01 to 2.00  $\text{mm}^{-1}$  incremented by 0.01  $\text{mm}^{-1}$ . The resulting misfit was quantified using sum of squares for all  $n$  slices, weighted by  $L_N/T_N$  error,  $\sigma$ :

$$SSE = \sum_{i=1}^n \frac{\left( \left[ \frac{L_N}{T_N} \right]_{\text{measured}} - \left[ \frac{L_N}{T_N} \right]_{\text{simulated}} \right)^2}{\sigma^2} \quad \text{Eq. 4}$$

SSE values are plotted as a function of  $\overline{\sigma\varphi_0}$  and  $\mu$  values in **Figure 3**. Best-fit values for  $\overline{\sigma\varphi_0}$  are 1550 and 650  $\text{ka}^{-1}$  for the  $\text{IR}_{50}$  and  $\text{pIRIR}_{225}$  signals, respectively, with  $\mu$  values of 0.32 and 0.54  $\text{mm}^{-1}$ . These values indicate greater detrapping rates and sunlight penetration depths for the  $\text{IR}_{50}$  signal, consistent with previous work (Jenkins et al., 2018; Ou et al., 2018).

Assuming the bleaching kinetics for the core top samples are similar to KAY-110 (Glignani et al., 2019; Lehmann et al., 2018; Meyer et al., 2018), we can model the depth of bleaching that would result from various prescribed sunlight exposure durations. Predicted luminescence profiles for sunlight exposures lasting 1, 10, 50, and 100 ka are shown along with the steady state profile in **Figure 4**. For comparison, the  $\text{IR}_{50}$  and  $\text{pIRIR}_{225}$  signals from sample 19-KP-H1 are also plotted.

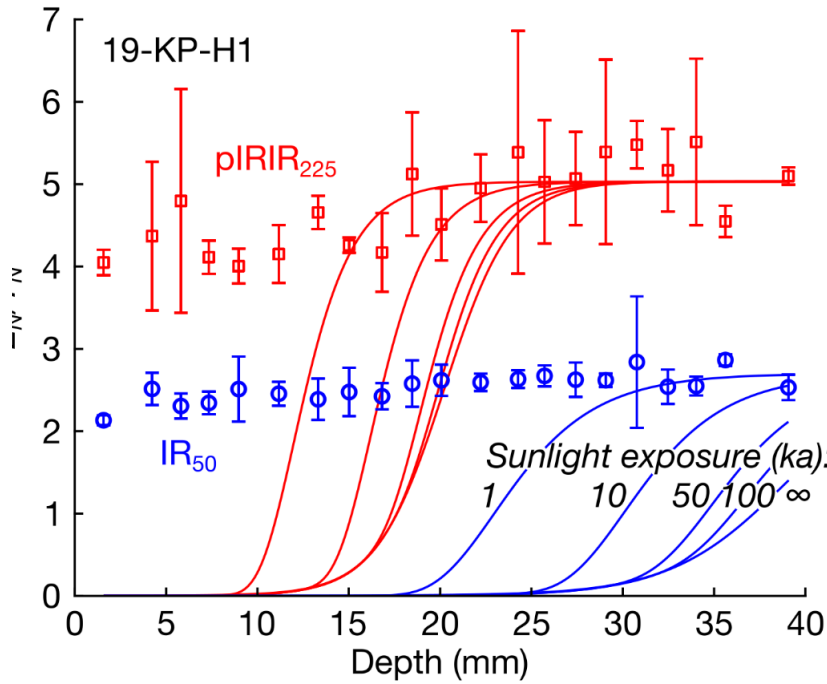


**Figure 4:** Comparison of luminescence depth profiles simulated for 1, 10, 50, 100 ka and infinite sunlight exposure with  $IR_{50}$  and  $pIRIR_{225}$  results from 19-KP-H1. The sampled depth interval would contain unbleached  $pIRIR_{225}$  and unbleached-to-partially-bleached  $IR_{50}$  signals between ~30 and 40 mm, regardless of bleaching duration.

The critical observation from **Figure 4** is that regardless of how long either surface may have been exposed to sunlight in the past, within the depth interval from 3 to 4 cm, the  $pIRIR_{225}$  signal will remain entirely unbleached and  $IR_{50}$  signal will be incompletely bleached. By comparison, both signals will be entirely bleached within the uppermost cm after an exposure as brief as 1 ka. This implies that we can test whether either core top was exposed to sunlight in the past by examining whether the apparent age within the uppermost 1 cm is younger than the apparent age at depths between 3 and 4 cm. We perform this test in the following section.

### Demonstrating field saturation

On initial inspection, luminescence depth profiles from both core top samples are apparently near or at field saturation, consistent with no recent sunlight exposure (Fig. 2 of main text). To test this assumption, we calculated the fading-corrected ages of three slices within the upper centimeter of the 19-KP-H1 core top and three slices between depths of 3 and 4 cm beneath the surface (slices indicated with asterisks in Table S2) to test whether shallow and deep ages can be distinguished. If the shallow ages are younger than the ages at depth, this would estimate the timing of most recent sunlight exposure. To determine the age of alkali feldspar samples, we must calculate the geologic dose rate (section 3), the equivalent dose, and the signal fading characteristics.

For equivalent dose determination (prior to necessary fading correction), aliquots were measured using a single aliquot regenerative (SAR) protocol (Wintle and Murray, 2006), shown in Table S2. After the natural measurement cycle, regenerative doses were 59, 117, 235, 470, 940, 1879, 0, and 59 Gy. Two aliquots each were measured for slices 1, 4, and 5, and one aliquot each was measured for slices 18, 19, 21 (Table S2). Results for the  $IR_{50}$  signals are shown in the right-hand columns of **Figures 5 and 6**, with the natural response ( $L_N/T_N$ ) plotted as a horizontal red line (dashed lines for  $1\sigma$  errors) and the regenerative dose responses given as blue circles. Note that the each row in **Figures 5 and 6** is a unique aliquot position (p. 9, p. 11, and so on) with the corresponding depth range given.

To quantify signal fading, aliquots were given a regenerative dose of 59 Gy, preheated to 250 °C for 100 s (Auclair et al., 2003) and then held at room temperature for effective delay times (Huntley and Lamothe, 2001) ranging from several minutes to several days (left-hand columns of **Figures 5 and 6**). The  $L/T$  ratios plotted against effective delay time,  $t$ , were regressed to determine the dimensionless recombination center density,  $\rho'$  ( $\pm 1\sigma$ ), using the expression of Kars et al. (2008):

$$\frac{L}{T} = \left(\frac{L}{T}\right)_0 \exp\left(-\rho' [\ln \ln \{1.8st\}]^3\right) \quad \text{Eq. 5}$$

where  $\left(\frac{L}{T}\right)_0$  is the prompt luminescence response and the frequency factor  $s$  is taken as  $3 \times 10^{15} \text{ s}^{-1}$  (Huntley, 2006).

The best-fit  $\rho'$  values were then used to construct growth response points without anomalous fading effects. These 'unfaded' dose response points were then fitted to a general-order kinetics dose-response function (Guralnik et al., 2015):

$$\frac{L}{T} = \left(\frac{L}{T}\right)_{\max} \left(1 - \left[1 + \frac{cD}{D_0}\right]^{-\frac{1}{c}}\right) \quad \text{Eq. 6}$$

where the kinetic order of trapping,  $\alpha = (c - 1)$  and  $\left(\frac{L}{T}\right)_{\max}$  is the asymptote of  $L/T$  at high doses. This was done 500 times for randomly selected values of  $\rho'$  drawn from a normal distribution, defined based on the fading regression. The resulting dose-response curves are plotted in grey in **Figures 5 and 6** and yield the unfaded characteristic dose value,  $D_0$  (Gy), for each aliquot.

The natural dose response curve is simulated according the best-fit values for  $\rho'$ ,  $D_0$  and  $\alpha$ , as well as the geologic dose rate,  $\dot{D}$ , assuming recombination by tunneling to the nearest neighbor at dimensionless distance,  $r'$  (Huntley, 2006):

$$\frac{d}{dt} \left( \frac{n}{N} [r'] \right) = \frac{\dot{D}}{D_0} \left( 1 - \frac{n}{N} [r'] \right)^\alpha - s \cdot e^{-\rho'^{-1/3} r'} \left( \frac{n}{N} [r'] \right) \quad \text{Eq. 7}$$

The resulting natural growth curves ( $n = 500$ ) are plotted in red in **Figures 5 and 6**. The fading-corrected age for each Monte Carlo iteration is the simulated age that reproduces the observed  $L_N/T_N$  ratio.

The order of trapping,  $\alpha$ , was restricted to the range (1, 2] and all but one aliquot yielded a value of 2. This is significant because proposed upper limit for equivalent dose determination of  $D_e < 2D_0$  (Wintle and Murray, 2006) assumes first-order growth ( $\alpha = 1$ ). By fitting to a second-order growth expression, our calculated  $2D_0$  values will indicate that we can resolve older ages than if we had fit to first-order dose response curves, though discrepancies between laboratory dose response curves and geologically constrained natural dose response datasets suggest apparent higher-order growth may be artificial (Timar-Gabor and Wintle, 2013). To avoid this pitfall, rather than estimating whether ages are greater than  $2D_0/\dot{D}$  (which, we estimate whether the shallow-core and deep-core ages are greater than an arbitrary upper-limit age. We choose a conservative value of 130 ka. For all aliquots, the percentage of Monte Carlo runs with  $IR_{50}$  ages  $> 130$  ka are indicated in the upper-left corners of the dose response plots in **Figures 5 and 6**.

Of the nine tested aliquots, seven consistently yield ages older than this threshold. Aliquot positions 9 and 27, which represent depths of [0 – 3.15 mm] and [33.37 – 34.67 mm] deviate from this, with highly scattered age values. This is due to the poorly constrained  $\rho'$  values determined based on the fading measurements from these two aliquots. Likewise, the natural test dose signal-to-background intensity was at least two-fold lower than the other aliquots. For the seven other aliquots, there is no difference in age between the shallow and deep depth intervals and the fading-corrected age for both is > 130 ka, indicating no sunlight exposure since at least 130 ka.

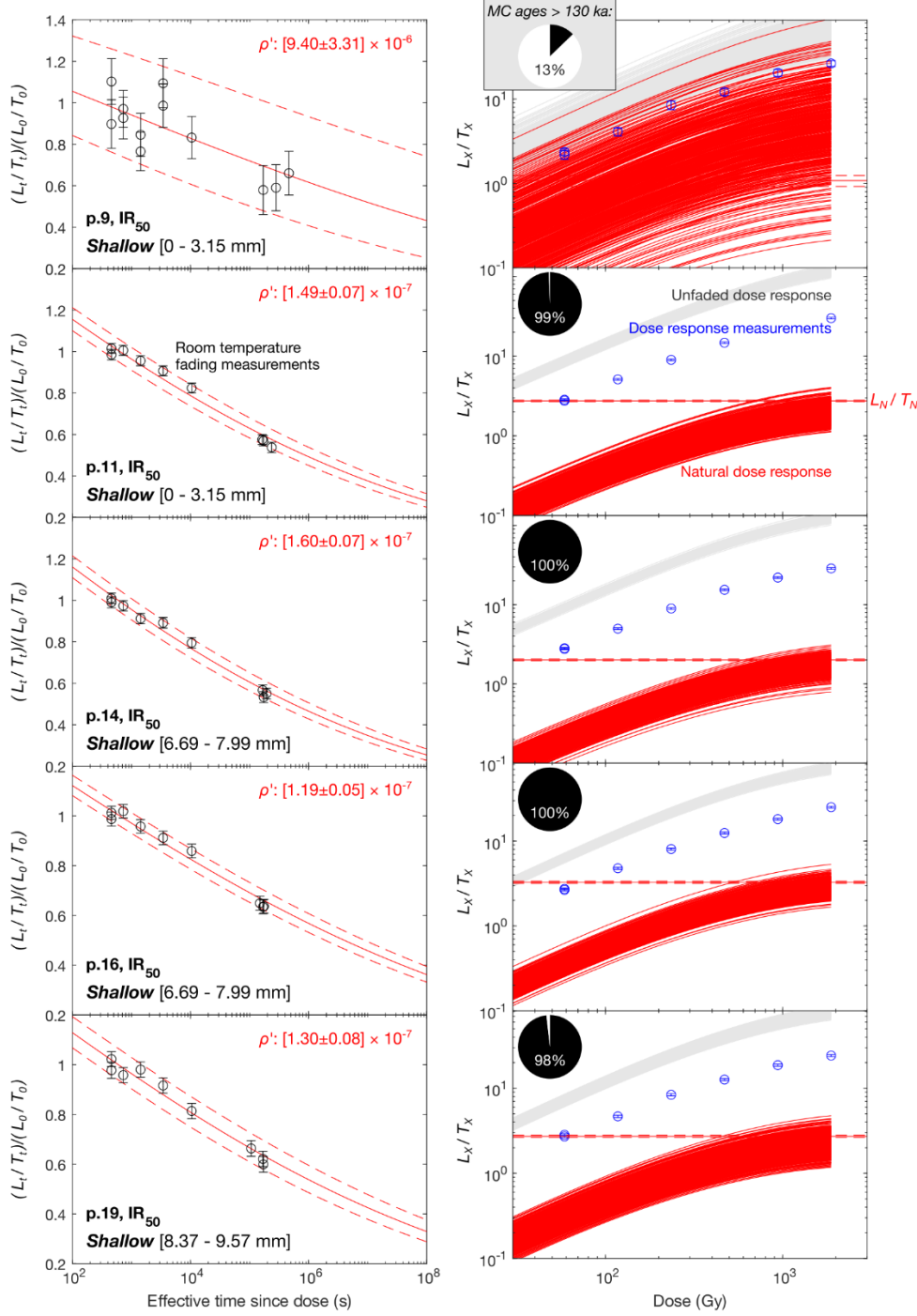


**Figure 5:** Room temperature fading measurements (left) and dose response measurements (right) for the  $IR_{50}$  signals are shown for the first five aliquots (row per aliquot, depth of each aliquot is given at bottom left). The fading measurements are regressed to Eq. 5 to determine the shown  $\rho'$  values. Using these values ( $\pm 1\sigma$ ), the measured dose response points (blue circles) are unfaded and then fit to a general-order kinetics growth curve (grey curves) to determine the characteristic dose,  $D_0$  (Gy). The red growth curves show the L/T response simulated at geologic dose rates, which can be compared against the measured natural luminescence response,  $L_N/T_N$  ( $\pm 1\sigma$ ), indicated by the horizontal red lines. 500 Monte Carlo iterations are shown for the unfaded and natural growth curve simulations. In the upper-left corner of the dose-response plots, the percentage of Monte Carlo iterations yielding an age > 130 ka is shown.

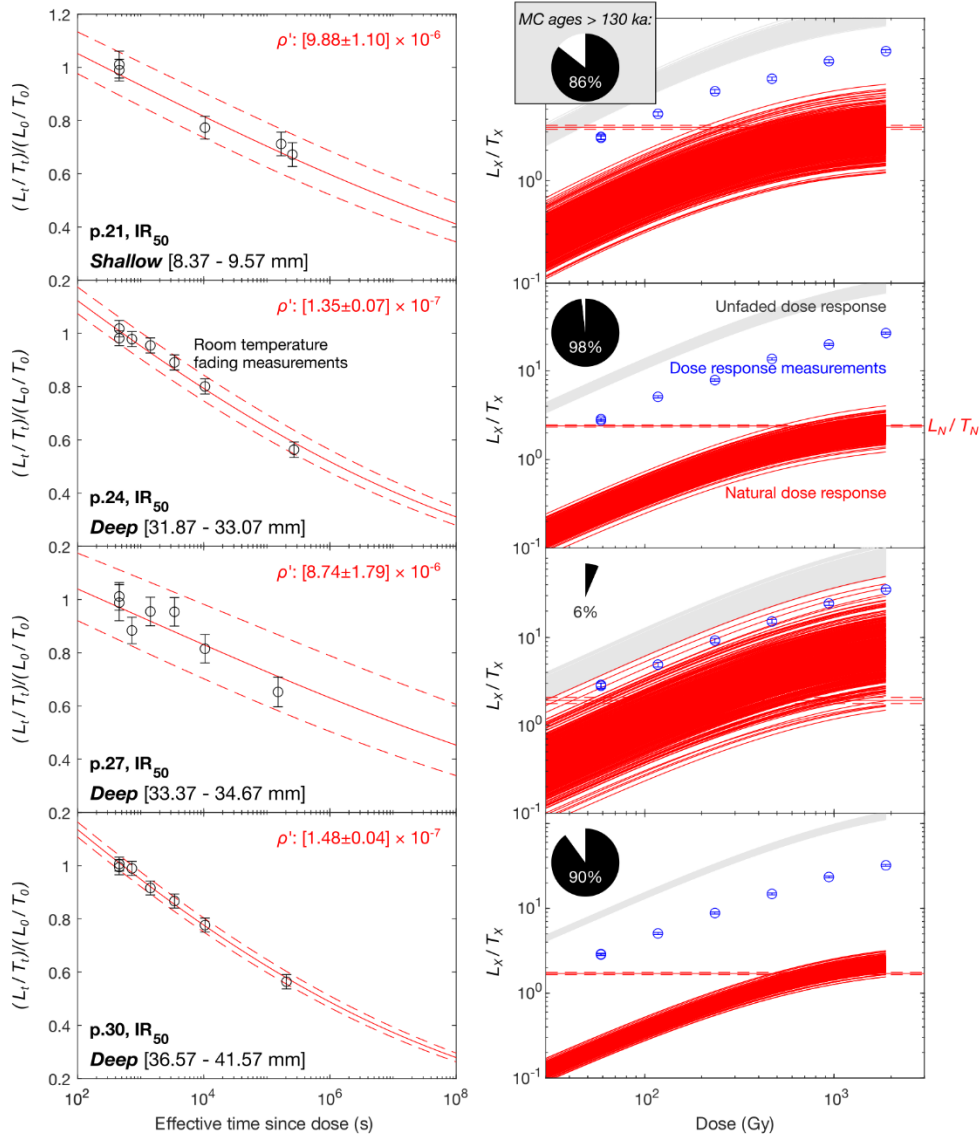


**Figure 6:** The last four aliquots are shown here. The figure meaning is the same as in Figure 5.

## References

- Auclair, M., Lamothe, M., and Huot, S., 2003, Measurement of anomalous fading for feldspar IRSL using SAR: Radiation Measurements, v. 37, p. 487-492.
- Balescu, S., and Lamothe, M., 1994, Comparison of TL and IRSL age estimates of feldspar coarse grains from waterlain sediments: Quaternary Science Reviews, v. 13, p. 437-444.
- Brennan, B. J., Lyons, R. G., and Phillips, S. W., 1991, Attenuation of alpha particle track dose for spherical grains: Nuclear Tracks and Radiation Measurements, v. 18, p. 249-253.
- Buylaert, J. P., Murray, A. S., Thomsen, K. J., and Jain, M., 2009, Testing the potential of an elevated temperature IRSL signal from K-feldspar: Radiation Measurements, v. 44, no. 5-6, p. 560-565.

Bøtter-Jensen, L., Andersen, C. E., Duller, G. A. T., and Murray, A. S., 2003, Developments in radiation, stimulation and observation facilities in luminescence measurements: *Radiation Measurements*, v. 37, p. 535-541.

Durcan, J. A., King, G. E., and Duller, G. A. T., 2015, DRAC: Dose Rate and Age Calculator for trapped charge dating: *Quaternary Geochronology*, v. 28, p. 54-61.

Gliganic, L. A., Meyer, M. C., Sohbati, R., Jain, M., and Barrett, S., 2019, OSL surface exposure dating of a lithic quarry in Tibet: Laboratory validation and application: *Quaternary Geochronology*, v. 49, p. 199-204.

Guralnik, B., Li, B., Jain, M., Chen, R., Paris, R. B., Murray, A. S., Li, S.-H., Pagonis, V., Valla, P. G., and Herman, F., 2015, Radiation-induced growth and isothermal decay of infrared-stimulated luminescence from feldspar: *Radiation Measurements*, v. 81, p. 224-231.

Guérin, G., Mercier, N., Nathan, R., Adamiec, G., and Lefrais, Y., 2012, On the use of the infinite matrix assumption and associated concepts: A critical review: *Radiation Measurements*, v. 47, no. 9, p. 778-785.

Huntley, D. J., 2006, An explanation of the power-law decay of luminescence: *Journal of Physics: Condensed Matter*, v. 18, no. 4, p. 1359-1365.

Huntley, D. J., and Baril, M. R., 1997, The K content of the K-feldspars being measured in optical dating or in thermoluminescence dating: *Ancient TL*, v. 15, no. 1, p. 11-13.

Huntley, D. J., and Lamothe, M., 2001, Ubiquity of anomalous fading in K-feldspars and the measurement and correction for it in optical dating: *Canadian Journal of Earth Sciences*, v. 38, no. 7, p. 1093-1106.

Jenkins, G. T. H., Duller, G. A. T., Roberts, H. M., Chiverrell, R. C., and Glasser, N. F., 2018, A new approach for luminescence dating glaciofluvial deposits -- high precision optical dating of cobbles: *Quaternary Science Reviews*, v. 192, p. 263-273.

Kars, R. H., Wallinga, J., and Cohen, K. M., 2008, A new approach towards anomalous fading correction for feldspar IRSL dating--tests on samples in field saturation: *Radiation Measurements*, v. 43, p. 786-790.

Lehmann, B., Valla, P. G., King, G. E., and Herman, F., 2018, Investigation of OSL surface exposure dating to reconstruct post-LIA glacier fluctuations in the French Alps (Mer de Glace, Mont Blanc massif): *Quaternary Geochronology*, v. 44, p. 63-74.

Liritzis, I., Stamoulis, K., Papachristodoulou, C., and Ioannides, K., 2013, A re-evaluation of radiation dose-rate conversion factors: *Mediterranean Archaeology and Archaeometry*, v. 13, p. 1-15.

Meyer, M. C., Gliganic, L. A., Jain, M., Sohbati, R., and Schmidmair, D., 2018, Lithological controls on light penetration into rock surfaces--Implications for OSL and IRSL surface exposure dating: *Radiation Measurements*, v. 120, p. 298-304.

Ou, X. J., Roberts, H. M., Duller, G. A. T., Gunn, M. D., and Perkins, W. T., 2018, Attenuation of light in different rock types and implications for rock surface luminescence dating: *Radiation Measurements*, v. 120, p. 305-311.

Sellwood, E. L., Guralnik, B., Kook, M., Prasad, A. K., Sohbat, R., Hippe, K., Wallinga, J., and Jain, M., 2019, Optical bleaching front in bedrock revealed by spatially-resolved infrared photoluminescence: Scientific Reports, v. 9, p. 2611.

Sohbat, R., Jain, M., and Murray, A., 2012, Surface exposure dating of non-terrestrial bodies using optically stimulated luminescence: A new method: Icarus, v. 221, p. 160-166.

Sohbat, R., Liu, J., Jain, M., Murray, A., Egholm, D., Paris, R., and Guralnik, B., 2018, Centennial- to millennial-scale hard rock erosion rates deduced from luminescence-depth profiles: Earth and Planetary Science Letters, v. 493, p. 218-230.

Sohbat, R., Murray, A. S., Porat, N., Jain, M., and Avner, U., 2015, Age of a prehistoric "Rodedian" cult site constrained by sediment and rock surface luminescence dating techniques: Quaternary Geochronology, v. 30, p. 90-99.

Thomsen, K. J., Kook, M., Murray, A. S., and Jain, M., 2018, Resolving luminescence in spatial and compositional domains: Radiation Measurements, v. 120, p. 260-266.

Timar-Gabor, A., and Wintle, A. G., 2013, On natural and laboratory generated dose response curves for quartz of different grain sizes from Romanian loess: Quaternary Geochronology, v. 18, p. 34-40.

Wintle, A. G., and Murray, A. S., 2006, A review of quartz optically stimulated luminescence characteristics and their relevance in single-aliquot regeneration dating protocols: Radiation Measurements, v. 41, p. 369-391.